International Forum on Aeroelasticity and Structural Dynamics
IFASD 2024
17-21 June 2024, The Hague, The Netherlands

AEROTHERMOELASTICITY ANALYSIS OF HYPERSONIC VEHICLE BASED ON MESHFREE METHOD

Zhan Sun[1], Zhiqiang Wan[1], Xiaozhe Wang[*,2], Liang Ma[1], Chang Li[1]

[1] School of Aeronautic Science and Engineering, Beihang University, 37 Xueyuan Road, Haidian District, Beijing, P.R. China, 100191.
[2] Institute of Unmanned System, Beihang University, 37 Xueyuan Road, Haidian District, Beijing, P.R. China, 100191.

Keywords: Hypersonic vehicles, aerothermoelasticity, meshfree method

Abstract: During the flight, hypersonic vehicles are subject to severe aerodynamic heating. It is necessary to consider the close coupling between aerodynamics/structure/heat, which is complicated to a certain extent. The difficulty of introducing thermal effects into pneumatic/structural coupling analysis is that there is a large difference in time scale between thermal conduction analysis and aerodynamic/structural coupling analysis. Based on the finite element method, aero-structure-thermo coupling analysis methods for hypersonic aircraft are quite mature, but certain disadvantages exist in terms of analysis time consumption. The rapid analysis method based on the meshfree method can improve calculation efficiency and ensure the accuracy of analysis results.In this paper, when refer to the rudder surface components, the thermal conduction analysis and structural static analysis methods in the aero-structure-thermo coupling analysis framework are replaced with a meshfree method. By storing the static analysis stiffness matrix and transient thermal conductivity stiffness matrix in advance, a rapid aero-structure-thermo coupling analysis method with the basis of the meshfree method is formed to obtain surface pressure, heat flow, temperature distribution, and aerothermoelasticity elastic response. This paper verifies the effectiveness of the meshfree method under the comparison of the results of the traditional finite element method and the meshfree method. While the meshfree method greatly reduces the time required for analysis, it has a certain degree of accuracy as well. The analysis results show that the thermal environment has a great influence on structural deformation. When the structural rigidity is on the high level, the thermal deformation far exceeds the aerodynamic elastic deformation. In the aero-structure-thermo coupling analysis of hypersonic aircraft, the influence of the thermal environment shall be taken into consideration.

1 INTRODUCTION

Hypersonic vehicles are defined as vehicles with a flight Mach number greater than 5, which are capable of achieving hypersonic flight in the atmosphere and transatmosphere. Hypersonic vehicles integrate new technologies from a multitude of disciplines within the field of aerospace, represent the future direction of research and development within the field of aerospace, and are currently a research hotspot within the field of aerospace, with an increasingly fierce trend of competition on the global stage.

Modern hypersonic vehicles are typically designed with an integrated airframe and propulsion system. Due to the high Mach number and extended flight time, these vehicles are exposed to complex and harsh environments during flight. This results in intense aerodynamic heating

effects, which can cause the surface of the vehicle to gradually reach extreme temperatures. The intense aerodynamic heating effect on the surface of hypersonic vehicles results in a gradual transfer of heat from the surface of the structure to the interior of the structure. This heat transfer affects the structural strength of the vehicle and generates a series of flight safety problems. The aforementioned safety issues manifest primarily in the following manner: following the heating of the vehicle's surface, the internal structure is continuously heated by heat conduction, resulting in a continuous increase in temperature. This, in turn, affects the material properties of the internal structure, causing a decrease in structural stiffness and the generation of a non-uniform temperature field, which in turn causes thermal stresses within the structure, leading to further deformation and softening of the structure. This, in turn, has a detrimental effect on the flight performance and structural strength of hypersonic vehicles. This will have a significant impact on the flight performance and structural integrity of the hypersonic vehicle.

In comparison to traditional vehicles, the coupling relationship between aerodynamic, structural and thermal properties will be further reinforced. The thermo-aerodynamic elasticity problem is of significant importance, therefore it is essential to consider the thermo-aerodynamic elasticity effect in the design process of hypersonic vehicles. This necessitates the accurate prediction of aerodynamic force, aerodynamic heat, structural heat transfer, structural deformation, thermal stress and other factors during the flight process. Furthermore, the coupling relationship between the multiple fields of flow, heat and structure must be fully considered, as well as the coupling relationship between flow, heat and structure, and multi-field coupling analysis must be carried out. It is therefore of great significance to study the thermo-aerodynamic problems of hypersonic vehicles through numerical simulation, which will help to improve the efficiency at the early stage of design and enhance the overall performance of hypersonic vehicles.

Hypersonic velocities exhibit a multitude of complex flow characteristics, including real gas effects, chemical reactions, viscous interferences, and so forth. Consequently, accurately predicting aerodynamic heating remains a complex and challenging problem. The study of the hypersonic thermal environment is primarily concerned with the calculation of the flow field outside the structure, as well as heat transfer calculations within the structure. At present, the analysis and calculation of hypersonic flow fields are mainly divided into two categories: numerical simulation (CFD) and engineering algorithms. At present, the numerical simulation of hypersonic flow fields remains a significant challenge in the field of computational fluid dynamics (CFD), largely due to the influence of discrete formats, grid distributions, numerical formats and convergence processes. In comparison to CFD numerical simulation methods, the utilisation of engineering algorithms to compute hypersonic non-stationary aerodynamic forces and aerodynamic heat is a more efficient and accurate approach, which is widely employed in early research and continues to evolve. Piston theory is currently the most prevalent approach for approximating hypersonic non-stationary aerodynamic forces. The method was initially proposed by Lighthill[1] and Ashley[2] et al. in the 1950s for non-constant aerodynamic calculations based on thin airfoil assumptions, with an applicable Mach number of 2.5-5.0. Since then, it has been improved to be applicable to a larger range of Mach numbers. McNamara[3] derived a semi-empirical formula for the displacement thickness of the boundary layer based on the laminar flow state of a flat plate at weak viscous disturbances as a means of correcting the effective shape of the vehicle. This was then used in conjunction with piston theory to solve for the non-constant aerodynamic forces based on the corrected shape. Meijer[4] conducted a comparison of several aerodynamic algorithms and discussed and analysed the scope of higher order piston aerodynamic applications. The principal engineering methodologies employed for the calculation

of hypersonic aerodynamic heat are the Eckert reference enthalpy method and the Spalding-Chi method for the calculation of surface heat flow density. D.E. Jarnette and Hamilton[5] developed a set of methods using axisymmetric simulation to calculate the laminar, turning, and turbulent heating rates of an arbitrary three-dimensional blunt head body in hypersonic flows. This was achieved by solving axisymmetric equations with known surface streamlines. McNamara[3] employed a Kriging proxy function to construct a hypersonic heat flow solution model for the purpose of computing the problem of predicting the thermal environment on the surface of hypersonic vehicle structures. As scholars continue to pay attention to the field of engineering algorithms, engineering methods now have high efficiency and reliable accuracy for solving related problems.

The hypersonic vehicle thermo-aerodynamic elasticity problem is a typical multi-field coupling analysis problem. The aerodynamic force, inertial force, and elastic force constitute the traditional aerodynamic elasticity problem. The aerodynamic heating constitutes the thermal environment. The aerodynamic force, inertial force, and elastic force exhibit varying degrees of strength in their coupling relationship with different physical quantities. This coupling relationship is illustrated in Figure 1. The figure illustrates that the physical fields of the traditional aeroelastic problem, comprising aerodynamic, inertial, and elastic forces, are strongly coupled to each other. In contrast, the aerodynamic heat is weakly coupled to the inertial force and strongly coupled to the elastic force. Consequently, when analysing the thermo-aerodynamic elasticity problem, it is essential to consider the impact of aerodynamic forces on the elasticity of the structure. On the one hand, aerodynamic heating will result in a significant alteration of the properties of the structural material, which will consequently influence the deformation of the structure. On the other hand, the formation of an inhomogeneous temperature field within the structure will give rise to the generation of thermal stresses, which will subsequently affect the structural mechanical properties. In the context of analysing coupling problems, it is appropriate to ignore those instances of weak coupling relationships with relatively minor impacts and instead focus on those instances of strong coupling relationships with a more pronounced impact.

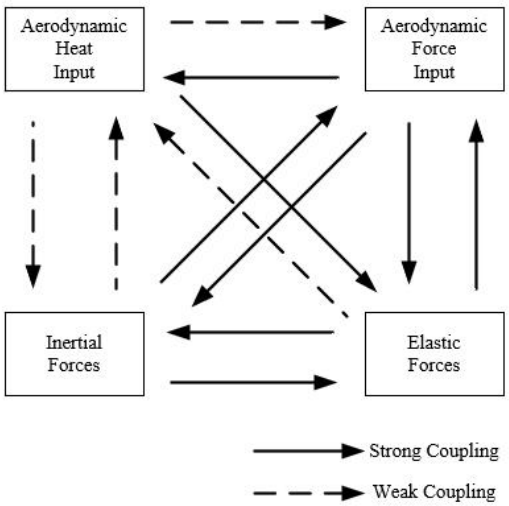

Figure 1 Coupling relations between different physical fields for thermo aerodynamic elasticity problems

2 THEORETICAL BASIS

2.1 Aerodynamic calculation methods

The piston theory of local flow was initially developed by Lighthill M. J. in the 1950s for the calculation of non-constant aerodynamic forces, with the fundamental assumptions of 1) thin airfoils and 2) high flight Mach numbers. The piston theory of hypersonic flow posits that the pressure exerted on the surface of an airfoil is solely contingent upon the normal velocity at that point.

The local instantaneous pressure acting on the piston surface can be derived from the principle of conservation of momentum and the isentropic equation:

$$\frac{p}{p_\infty}=\left(1+\frac{\gamma-1}{2}\frac{v_n}{a_\infty}\right)^{\frac{2\gamma}{(\gamma-1)}}$$

The Taylor expansion of the aforementioned equation, retaining the third order, is designated as the third-order piston theory. This results in the expression for the pressure coefficient of the third-order piston theory, which is given by:

$$C_p=\frac{2}{Ma_\infty^2}\left[\frac{v_n}{a_\infty}+\frac{(\gamma+1)}{4}\left(\frac{v_n}{a_\infty}\right)^2+\frac{(\gamma+1)}{12}\left(\frac{v_n}{a_\infty}\right)^3\right]$$

2.2 Pneumatic thermal calculation method

The majority of aerodynamic thermal calculations are based on the Eckert reference method, the Reynolds ratio simulation method and the flat plate heat flow formula. The coefficient of friction for the boundary layer of an incompressible laminar flow is:

$$C_f=\frac{\tau}{\frac{1}{2}\rho u_e^2}=2f''(0)\sqrt{\frac{\mu}{u_e x}}=\frac{2f''(0)}{\sqrt{\mathrm{Re}_x}}=\frac{0.664}{\sqrt{\mathrm{Re}_x}}$$

Where $\mathrm{Re}_x=\frac{\rho u_e x}{\mu}$ is the Reynolds number at the coordinates.

The principal objective of the Eckert reference method is to adapt the aforementioned formula for the friction resistance of incompressible flow in order to facilitate its application to the calculation of the friction resistance of compressible flow. The formula is as follows:

$$T^*=0.5T_w+0.22T_r+0.28T_e$$

Once the reference temperature has been obtained, the temperature-dependent quantities in the unpressurised flow must also be determined from the reference temperature. The reference viscosity coefficient and reference density can be determined from the equation of state and the Satran formula, which can be substituted into the friction coefficient formula to find the friction coefficient of the unpressurised flow.

$$\mu^* = (\frac{T^*}{288.15})^{1.5} \frac{398.55}{T^* + 110.4} \times 1.7894 \times 10^{-5}$$

$$\rho^* = \frac{p_e}{RT^*}$$

The following wall heat transfer coefficients can be derived using the Reynolds comparison method, where Pr is the Prandtl number.

$$St = \frac{0.332\,\mathrm{Pr}^{1/3}}{\mathrm{Pr}\sqrt{\mathrm{Re}_x}} = \frac{0.332}{\mathrm{Pr}^{2/3}\sqrt{\mathrm{Re}_x}}$$

The substitution of the aforementioned friction coefficients yields the following result:

$$St = \frac{C_f}{2\,\mathrm{Pr}^{2/3}}$$

The final heat flow into the structure can be obtained by combining the flat plate heat flow equation and the radiative heat dissipation equation. The Stanford constant, which is equal to 5.669E-8 W/m2/T4, represents the radiative emissivity of the non-blackbody surface.

$$Q_{aero} = \rho_e u_e c_p \left(T_r - T_w\right) St^*$$

$$Q_{rad} = \sigma\varepsilon(T_w^4 - T_\infty^4)$$

$$Q = Q_{aero} - Q_{rad}$$

3 MESHFREE METHOD THEORY

3.1 Fundamental equations for two-dimensional solids

The static equilibrium equations and constraints for the two-dimensional solid model are as follows: Ω represents the problem domain, Γ_u is the displacement boundary condition, Γ_t is the force boundary condition, and **b** is the external force vector.

$$\begin{cases} \mathbf{L}^T\boldsymbol{\sigma} + \mathbf{b} = 0 & \text{in } \Omega \\ \mathbf{t} = \bar{\mathbf{t}} & \text{in } \Gamma_t \\ \mathbf{u} = \bar{\mathbf{u}} & \text{in } \Gamma_u \end{cases}$$

$\mathbf{L}$ is the matrix of differential operators:

$$\mathbf{L} = \begin{bmatrix} \frac{\partial}{\partial x} & 0 \\ 0 & \frac{\partial}{\partial y} \\ \frac{\partial}{\partial y} & \frac{\partial}{\partial x} \end{bmatrix}$$

The Galerkin weighted residual method and the principle of minimum potential energy can be employed to derive the global weak form equation of the above equation:

$$\int_{\Omega} (\mathbf{L}\delta\mathbf{u})^{\mathrm{T}} (\mathbf{D}\mathbf{L}\mathbf{u}) d\Omega - \int_{\Omega} \delta\mathbf{u}^{\mathrm{T}}\mathbf{b} d\Omega - \int_{\Gamma_t} \delta\mathbf{u}^{\mathrm{T}}\bar{\mathbf{t}} d\Gamma = 0$$

3.2 Integral domain discrete

The original problem can be transformed into a series of systems of equations by integrating the aforementioned global vulnerability equations over the background grid and boundary. Upon completion of the integration process, the function values at the point of interest are interpolated from the function values at the pre-arranged field nodes within a specified range proximate to the point of interest. This range is also referred to as the support domain of the point to be solved.

3.3 Integral domain discrete

The function value $\mathbf{U}_s$ for all field nodes can be expressed as a linear combination of the interpolated basis functions of the individual radial basis points:

$$\mathbf{U}_s = \mathbf{R}_0\mathbf{a} + \mathbf{P}_m\mathbf{b}$$

The $\mathbf{R}_0$ matrix is the one representing the radial basis functions, while the $\mathbf{P}_m$ matrix is the one representing the polynomial basis functions. The $\mathbf{a}$ and $\mathbf{b}$ vector coefficient matrices are the ones to be solved.

From the positive definite constraints, it is possible to derive m constraint equations.

$$\mathbf{P}_m^{\mathrm{T}}\mathbf{a} = 0$$

The union of the two matrices yields the following matrix equation:

$$\tilde{\mathbf{U}}_s = \begin{Bmatrix} \mathbf{U}_s \\ \mathbf{0} \end{Bmatrix} = \underbrace{\begin{bmatrix} \mathbf{R}_0 & \mathbf{P}_m \\ \mathbf{P}_m^{\mathrm{T}} & \mathbf{0} \end{bmatrix}}_{G} \begin{Bmatrix} \mathbf{a} \\ \mathbf{b} \end{Bmatrix} = \mathbf{G}\mathbf{a}_0$$

The solution provides the coefficient to be determined:

$$\mathbf{a}_0 = \begin{Bmatrix} \mathbf{a} \\ \mathbf{b} \end{Bmatrix} = \mathbf{G}^{-1}\tilde{\mathbf{U}}_s$$

Then for any point to be found, the function value $u(\mathbf{x})$ can be similarly expressed by the radial basis function as:

$$u(\mathbf{x}) = \mathbf{R}^{\mathrm{T}}(\mathbf{x})\mathbf{a} + \mathbf{p}^{\mathrm{T}}(\mathbf{x})\mathbf{b} = \{\mathbf{R}^{\mathrm{T}}(\mathbf{x}) \quad \mathbf{p}^{\mathrm{T}}(\mathbf{x})\}\mathbf{G}^{-1}\tilde{\mathbf{U}}_s = \tilde{\mathbf{\Phi}}^{\mathrm{T}}(\mathbf{x})\tilde{\mathbf{U}}_s$$

$$\begin{aligned}\tilde{\mathbf{\Phi}}^{\mathrm{T}}(\mathbf{x}) &= \{\mathbf{R}^{\mathrm{T}}(\mathbf{x}) \quad \mathbf{p}^{\mathrm{T}}(\mathbf{x})\}\mathbf{G}^{-1} \\ &= \{\phi_1(\mathbf{x}) \quad \phi_2(\mathbf{x}) \quad \cdots \quad \phi_n(\mathbf{x}) \quad \phi_{n+1}(\mathbf{x}) \quad \cdots \quad \phi_{n+m}(\mathbf{x})\}\end{aligned}$$

3.4 Integral domain discrete

In the context of a two-dimensional solid problem, the displacement vector $\mathbf{u}$ of the n field nodes in the domain of support can be used to represent the displacement $\mathbf{u}_g$ at any Gaussian integration point.

$$\mathbf{u}_g = \begin{Bmatrix} u \\ v \end{Bmatrix} = \begin{bmatrix} \phi_1 & 0 & \cdots & \phi_n & 0 \\ 0 & \phi_1 & \cdots & 0 & \phi_n \end{bmatrix} \begin{Bmatrix} u_1 \\ v_1 \\ \vdots \\ u_n \\ v_n \end{Bmatrix} = \mathbf{\Phi}_{(2\times 2n)}\mathbf{u}_{(2n\times 1)}$$

The terms in the global weak-form equation yield the following equation for any Gaussian integration point:

$$(\mathbf{L}\delta\mathbf{u})^{\mathrm{T}}\mathbf{D}\mathbf{L}\mathbf{u} = (\mathbf{B}\delta\mathbf{u})^{\mathrm{T}}\mathbf{D}\mathbf{B}\mathbf{u} = \delta\mathbf{u}^{\mathrm{T}}\underbrace{\mathbf{B}^{\mathrm{T}}\mathbf{D}\mathbf{B}}_{\mathbf{K}_g}\mathbf{u} = \delta\mathbf{u}^{\mathrm{T}}\mathbf{K}_g\mathbf{u}$$

$$\delta\mathbf{u}_g^{\mathrm{T}}\mathbf{b}_g = (\mathbf{\Phi}\delta\mathbf{u})^{\mathrm{T}}\mathbf{b}_g = \delta\mathbf{u}^{\mathrm{T}}\underbrace{\mathbf{\Phi}^{\mathrm{T}}\mathbf{b}_g}_{\mathbf{F}_g^b} = \delta\mathbf{u}^{\mathrm{T}}\mathbf{F}_g^b$$

$$\delta\mathbf{u}_g^{\mathrm{T}}\overline{\mathbf{t}}_g = (\mathbf{\Phi}\delta\mathbf{u})^{\mathrm{T}}\overline{\mathbf{t}}_g = \delta\mathbf{u}^{\mathrm{T}}\underbrace{\mathbf{\Phi}^{\mathrm{T}}\overline{\mathbf{t}}_g}_{\mathbf{F}_g^t} = \delta\mathbf{u}^{\mathrm{T}}\mathbf{F}_g^t$$

$\mathbf{K}_g$, $\mathbf{F}_g^b$ and $\mathbf{F}_g^t$ are the Gaussian integral point stiffness array, Gaussian integral point body force and surface force vectors, respectively.

The integration points are subjected to a series of operations. Firstly, the $\mathbf{K}_g$, $\mathbf{F}_g^b$ and $\mathbf{F}_g^t$ at each

point are multiplied by the weight factor and the determinant of the Jacobian matrix in accordance with the Gaussian integration formula. Secondly, these values are superimposed on the overall stiffness array and the overall force vector, with reference to the node numbering position.

Once the overall stiffness array has been obtained, the problem can be solved by imposing the displacement boundary conditions.

4 AEROTHERMOELASTICITY ANALYSIS OF RUDDER SURFACE BASED ON MESHFREE METHOD

4.1 Model description

In this paper, the geometric shape of a missile rudder is taken as a benchmark to establish a finite element model of the rudder.The geometrical parameters of the model are shown in Figure 1, with the wing root chord length c=740mm, leading edge swept back angle 56°, and the maximum thickness of the airfoil structure d=(52+4×2)mm, where 4×2 corresponds to the thickness of the single layer of the thermal protection layer on the upper and lower airfoils.

Hypersonic vehicles are subjected to severe aerodynamic heating during high-speed flight, resulting in a rapid increase in both the temperature of the flow field boundary layer and the internal structure. This necessitates the use of thermal insulation measures to protect the internal structure. Accordingly, a layer of thermal protection structure is positioned on the upper and lower surfaces of the rudder surface of the model in this paper, comprising a thermal protection layer (outer layer, thickness 2 mm) and a thermal insulation layer (inner layer, thickness 2 mm). The relationship between the arrangement of the thermal protection structure and the internal structure and the materials used is illustrated in Figure 2.

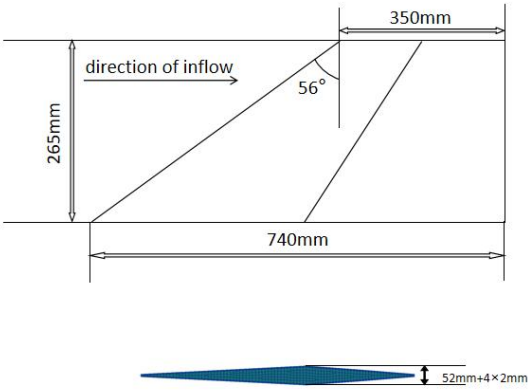

Figure 2 Schematic of rudder geometry parameters

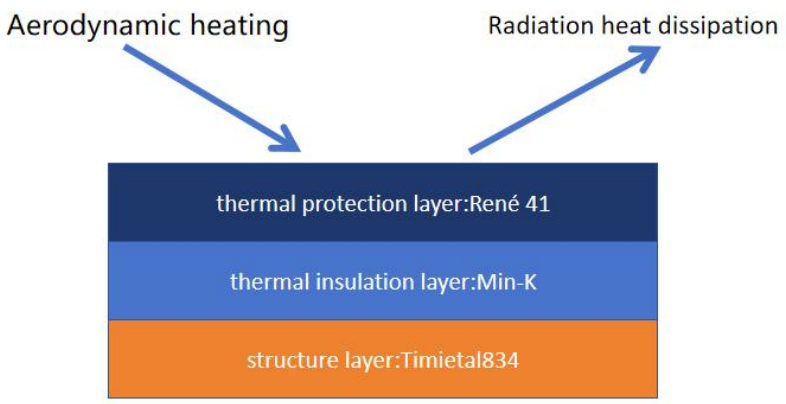

Figure 3 Schematic diagram of the thermal protection layer on the rudder surface

The properties of the aforementioned materials are presented in the table below. The designation "T-dep" (temperature dependency) indicates that the material property is temperature dependent. It should be noted that the Young's modulus of the insulating ceramic Min-K is generally not taken into account. In this paper, the properties of this material are directly set to 10 times those of the nickel-based alloy René 41 for convenience.

Table 1 Heat transfer and mechanical properties of materials used in the model

	Density	Young's modulus	Poisson's ratio	Coefficient of linear expansion	Thermal conductivity	Specific heat capacity
	kg/m^3	Pa		$1/K$	$W/m/K$	$J/kg/K$
René 41	8240	1.09e+11	0.31	1.1e-5	18	541
Min-K	256	1.09e+12	0.31	——	0.052	858
Timetal834	4550	T-dep	0.31	1.1e-5	7	525

The change in Young's modulus with temperature for the titanium alloy Timetal834 is illustrated in Figure 4.

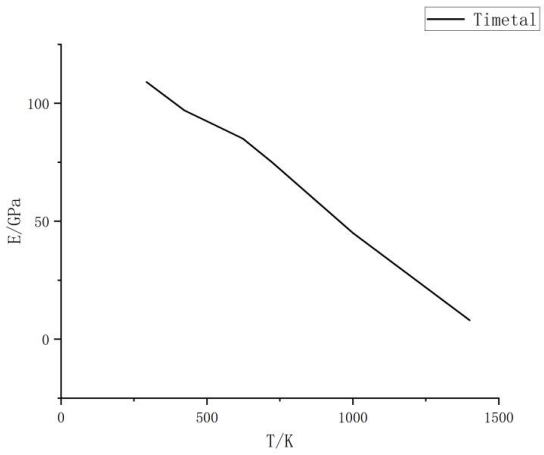

Figure 4 Young's modulus versus temperature for titanium alloys

Figure 5 illustrates the finite element model of the rudder, which comprises solid cells distributed throughout the entire rudder. The mesh number is 31750, with 36771 nodes, and the rudder is supported by solid constraints in the middle part of the rudder root. The aerodynamic mesh is identical to that used for the upper and lower surfaces of the rudder, and the background mesh and nodes employed for the meshfree method of analysis are identical to those used for the finite element mesh and nodes.

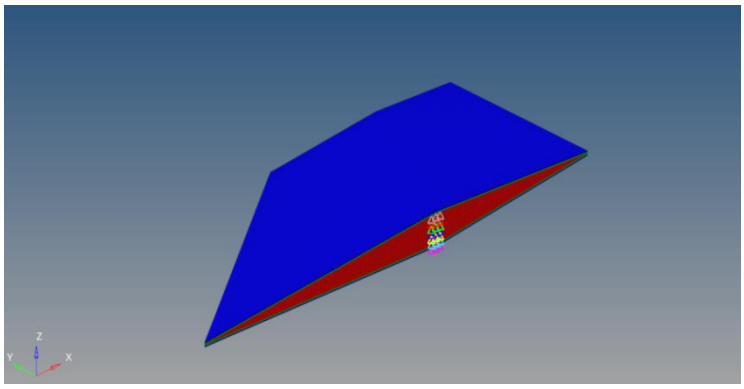

Figure 5 Diagram of rudder FEM model and constraints

4.2 Case and result analyses

The computational parameters of the case are as follows: a solid support constraint in the middle part of the rudder root, a flight Mach number of 6 Ma, a flight altitude of 15,000 m, and an angle of attack α=6°. The initial temperature of the structure is 300 K, the Prandtl number Pr = 0.86, the air specific heat ratio γ = 1.4, and the radiation emissivity ε = 0.85. The interval of the calculation of the aerodynamic heat flow and transient heat conduction is ΔT = 1 s, and the total calculation time is T = 300 s.

In accordance with the aforementioned model and calculation conditions, the finite element method and meshfree method were employed to analyse the rudder surface for thermal aeroelasticity. The respective calculation times for the finite element method and meshfree method were 23.36 hours and 3.77 hours. It was observed that the meshfree method analysis

resulted in enhanced calculation efficiency and a reduction in calculation time.

The results of surface pressure and heat flow distributions, aerodynamic and structural temperature distributions, temperature change processes at monitoring points, and rudder deformation resulting from the two methods will be compared and analysed in the following sections.

4.2.1 Pressure and heat flow distribution

At the outset, no differentiation is made between the outcomes of the two methodologies, as the aerodynamic and aerothermal calculation methods and input data are identical. Figure 6 to Figure 11 illustrate the pressure distribution on the upper and lower surfaces of the rudder at 0s and 300s, respectively. At the initial moment, only four different values appear on the upper and lower surfaces in both the front and back. This is because the piston theory is related to the slope of the surface mesh. Subsequently, the surface pressure shows an uneven distribution, with the maximum value appearing in the leading edge of the rudder's lower surface, as a result of the deformation of the structure.

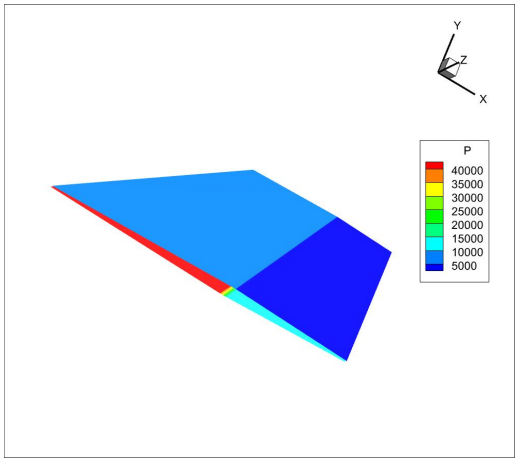

Figure 6 Upper surface pressure distribution at 0s

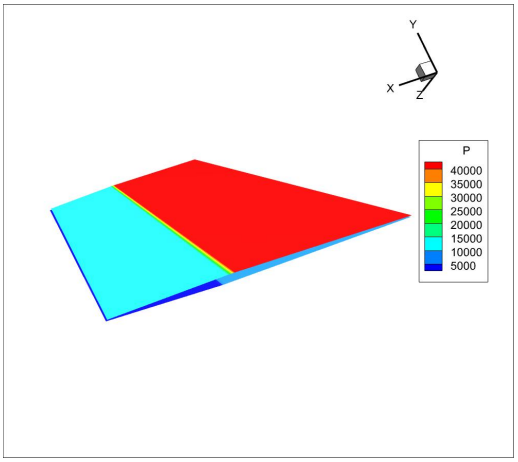

Figure 7 Lower surface pressure distribution at 0s

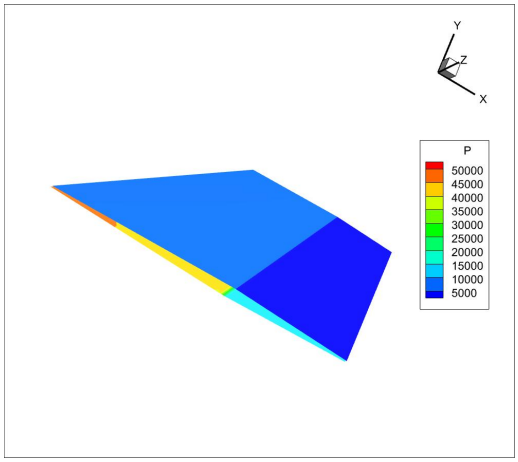

Figure 8 Upper surface pressure distribution at 300s by FEM

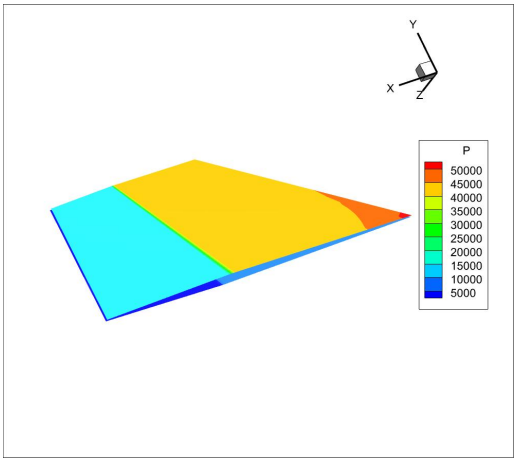

Figure 9 Lower surface pressure distribution at 300s by FEM

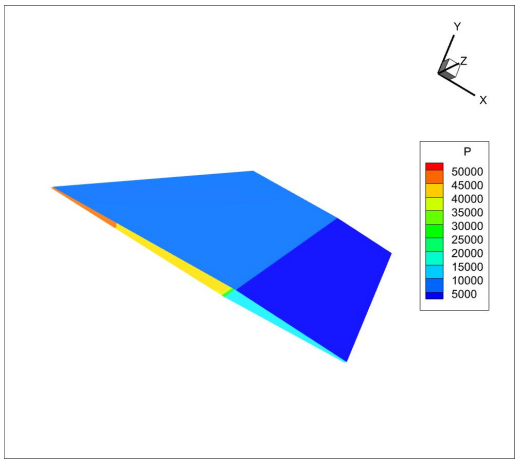

Figure 10 Upper surface pressure distribution at 300s by meshfree method

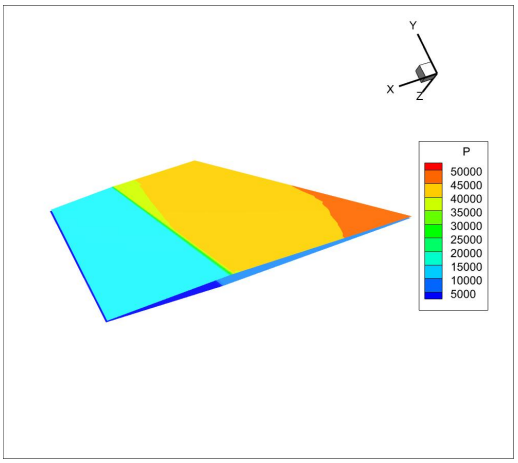

Figure 11 Lower surface pressure distribution at 300s by meshfree method

The distribution of heat flow on the upper and lower surfaces of the rudder at 0s and 300s is presented in Figure 12 to Figure 17 respectively. The initial heat flow is considerably greater than that observed at 300s. At this latter time point, the final heat flow distribution results are slightly different due to the differing calculation methods employed. Furthermore, as the flight time increases, the aerodynamic heating and radiative heat dissipation gradually tend to be balanced.

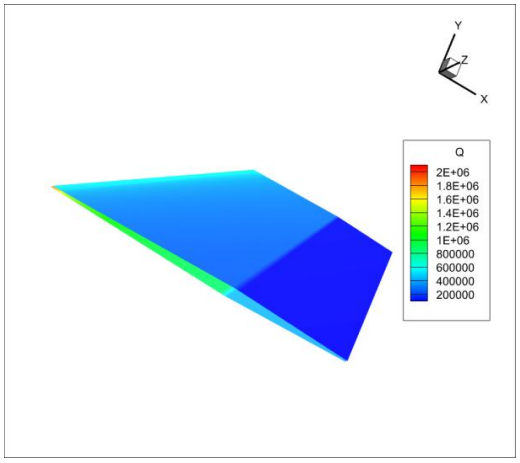

Figure 12 Upper surface heat flow distribution at 0s

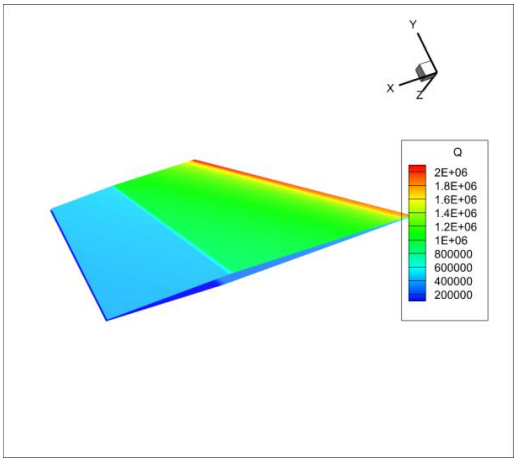

Figure 13 Lower surface heat flow distribution at 0s

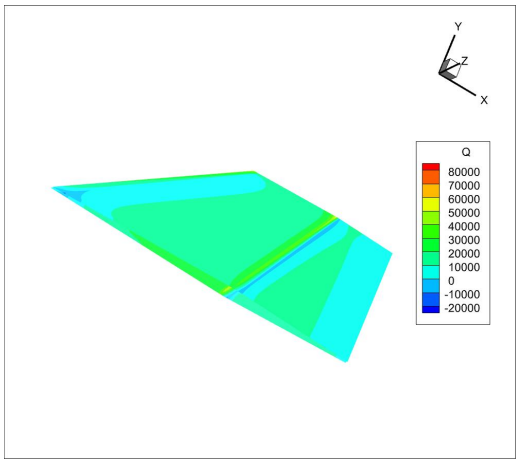

Figure 14 Upper surface heat flow distribution at 300s by FEM

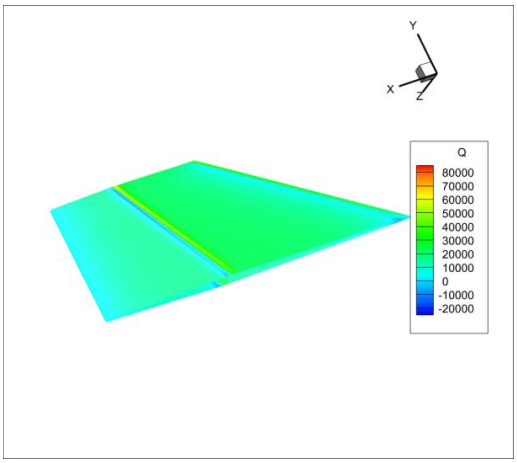

Figure 15 Lower surface heat flow distribution at 0s by FEM

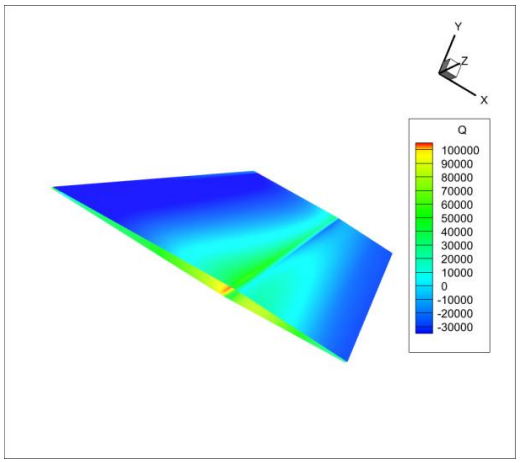

Figure 16 Upper surface heat flow distribution at 300s by meshfree method

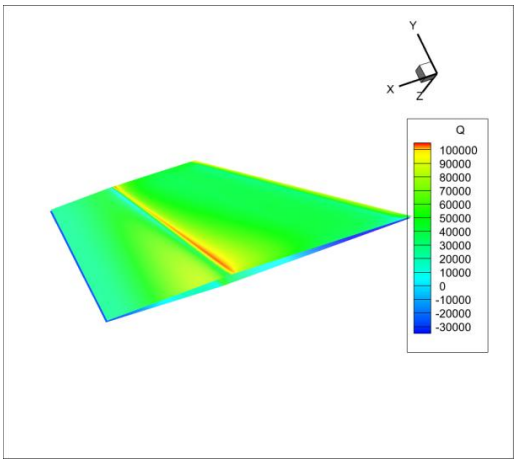

Figure 17 Lower surface heat flow distribution at 0s by meshfree method

4.2.2 Aerodynamic and structural temperature distribution

The temperature distributions of the aerodynamic surfaces for the finite element method and meshfree method at 300s are presented in Figure 18 to Figure 21, respectively. It can be observed that the surface temperature is considerably higher than the initial temperature throughout the hypersonic flight process. The aerodynamic heating effect is evident, with the lower surface temperature being higher than the upper surface temperature. The maximum temperature value is observed at the leading edge of the lower surface, reaching 1500K. The surface temperature distributions obtained by both methods are essentially identical.

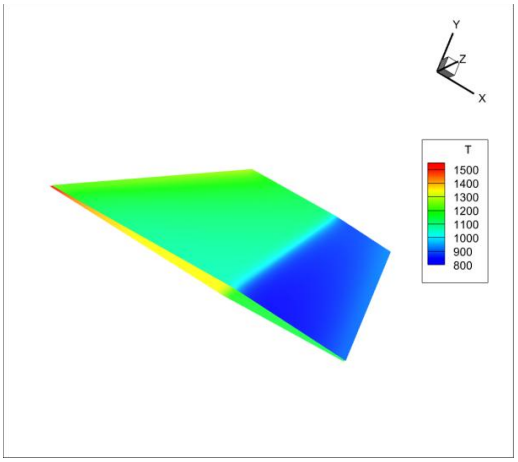

Figure 18 Upper aerodynamic surface temperature distribution at 300s by FEM

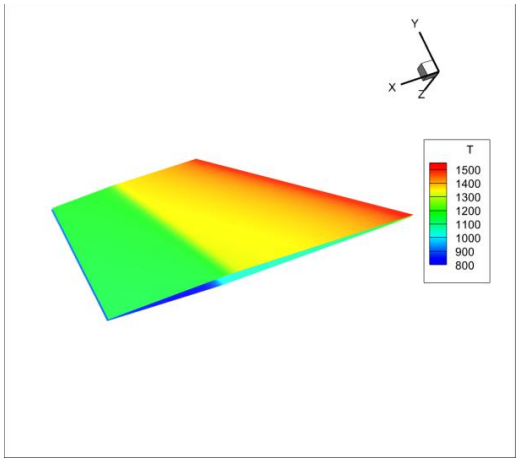

Figure 19 Lower aerodynamic surface temperature distribution at 300s by FEM

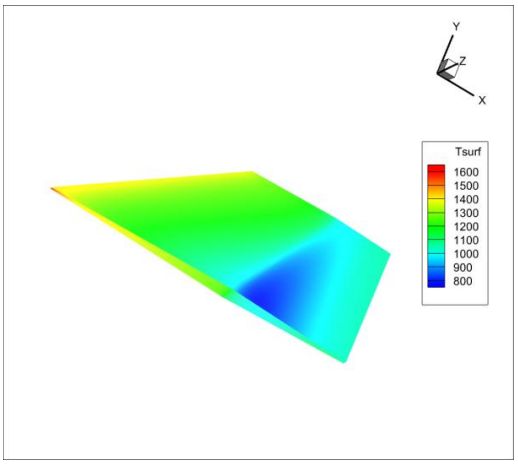

Figure 20 Upper aerodynamic surface temperature distribution at 300s by meshfree method

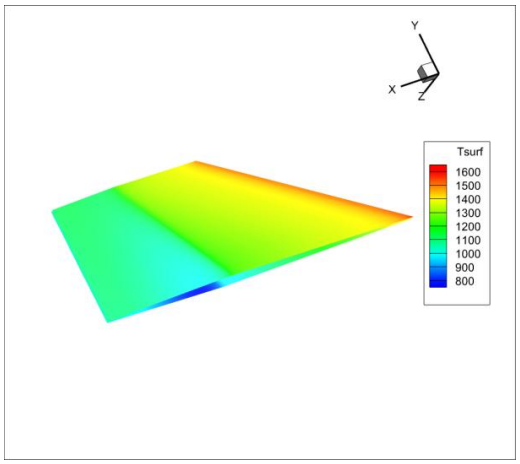

Figure 21 Lower aerodynamic surface temperature distribution at 300s by meshfree method

Figure 22 to Figure 25 illustrate the surface temperature distributions of the structural layer at 300 s for the finite element method and the meshfree method, respectively. The structural layer is defined as the internal structure, with the thermal shield and insulation removed. The protective effect of the thermal protective layer and the insulation layer is evident in the temperature distribution of the structural layer. The temperature in most areas of the structural layer is below 600 K, with only the temperature in the leading and trailing edge areas reaching 1,000 K. This is in contrast to the average temperature of 1,000 K on the aerodynamic surface, which demonstrates the significant protective effect of the thermal protective layer and the insulation layer.

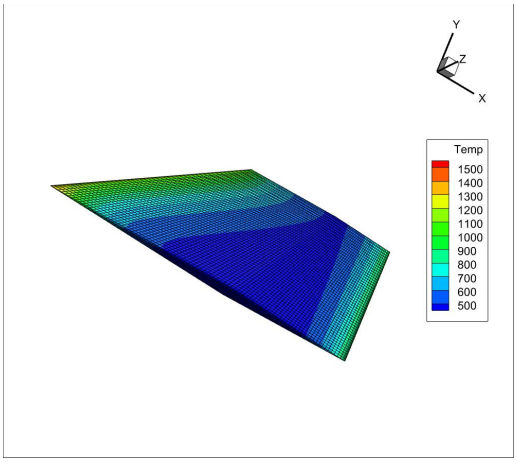

Figure 22 Upper structural layer surface temperature distribution at 300s by FEM

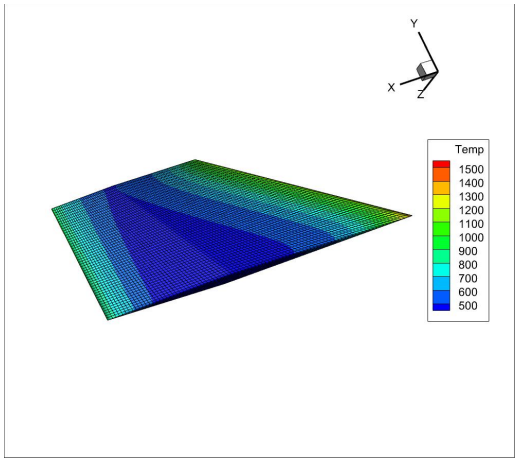

Figure 23 Lower structural layer surface temperature distribution at 300s by FEM

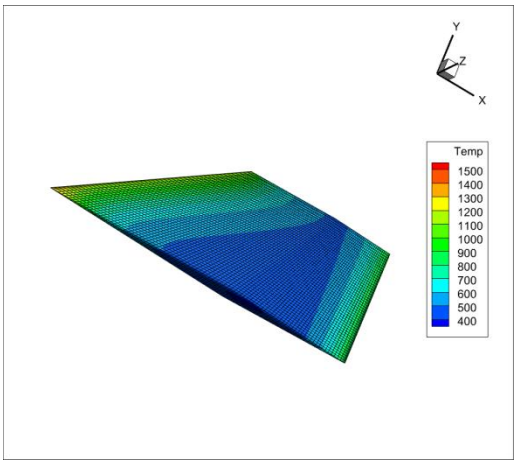

Figure 24 Upper structural layer surface temperature distribution at 300s by meshfree method

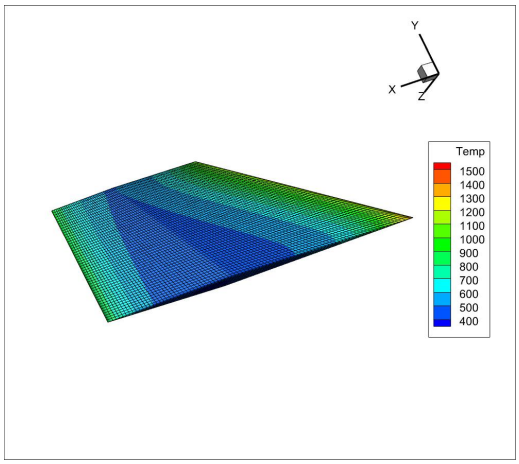

Figure 25 Lower structural layer surface temperature distribution at 300s by meshfree method

4.2.3 Temperature change processes at monitoring points

To provide further evidence of the temperature fluctuations that occur during flight, a number of monitoring points have been established on the aerodynamic surface and the structural layer, respectively. These points are used to monitor the temperature changes that occur during flight.

The temperature monitoring points are positioned at the leading edge, trailing edge, upper and lower vertices of the rudder root and tip, as illustrated in Figure 26 and Figure 27. These figures also show the locations of the upper and lower aerodynamic surface temperature detection points. Figure 28 to Figure 31 present the curves of the upper and lower surface monitoring point temperatures over time for the Finite Element Method (FEM) and the meshfree method. This is due to the fact that the heat flow on the lower surface is higher than that on the upper surface, resulting in a higher temperature at the monitoring point on the lower surface than at the upper surface. Furthermore, the temperature at the leading edge is greater than that at the upper surface. The temperature at the leading edge is greater than that at the trailing edge, and the temperature

at each point increases rapidly during the flight, reaching a stable value at the end.

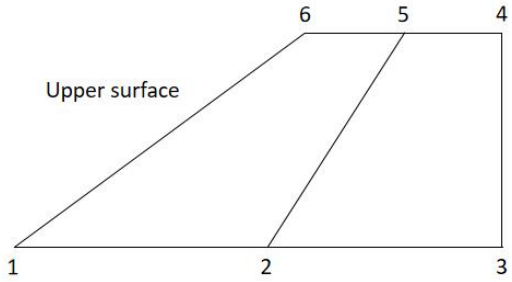

Figure 26 Aerodynamic monitoring point location on the upper surface

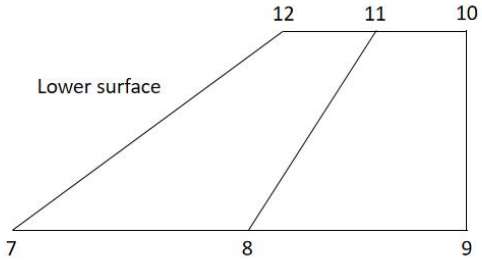

Figure 27 Aerodynamic monitoring point location on the lower surface

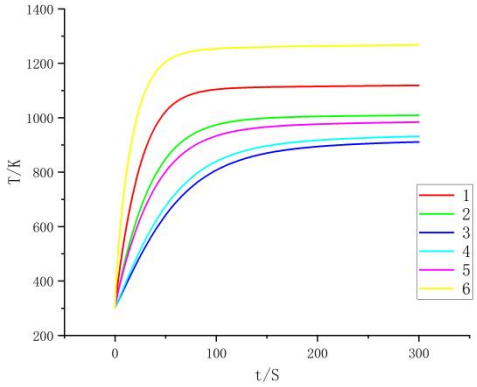

Figure 28 Temperature changes of monitoring points on the upper surface by FEM

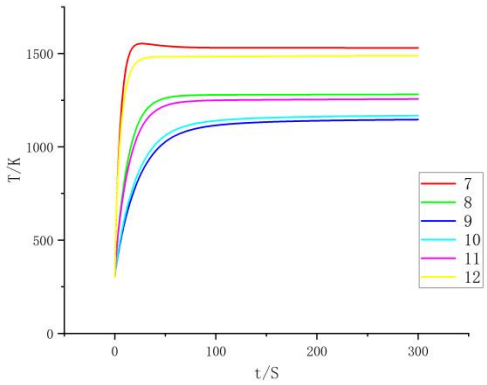

Figure 29 Temperature changes of monitoring points on the lower surface by FEM

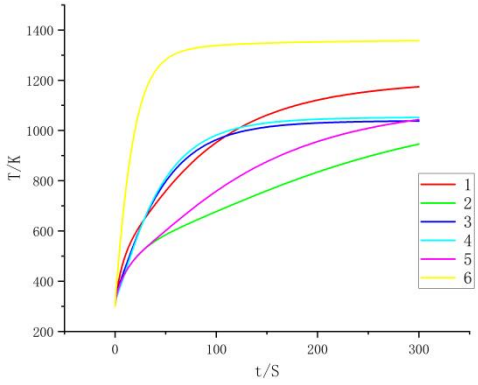

Figure 30 Temperature changes of monitoring points on the upper surface by meshfree method

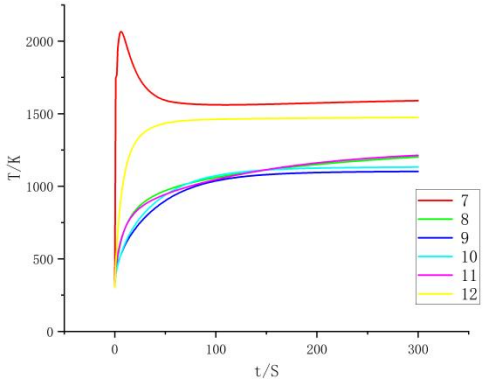

Figure 31 Temperature changes of monitoring points on the lower surface by meshfree method

The temperature monitoring points are positioned at the leading and trailing edges, as well as the upper and lower vertices of the root and tip of the structural layer, as illustrated in Figure 32 and Figure 33. The nodes numbered 5 and 7 indicate the lower vertices of the structure. Figure 34 and Figure 35 illustrate the temperature changes at the leading and trailing edge monitoring points and the upper and lower vertices, respectively. It can be observed that the temperature changes at the monitoring point locations, which are not shown repeatedly, are consistent between the meshfree and finite element methods. From the figures, it can be seen that the temperature at the leading and trailing edges is high and gradually converges to a stable value, while the temperature at the upper and lower vertices is relatively low and in a slowly increasing trend.

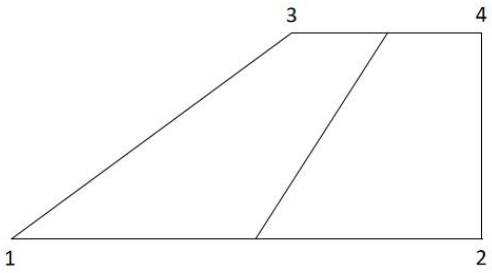

Figure 32 Diagram of the structure monitoring point locations

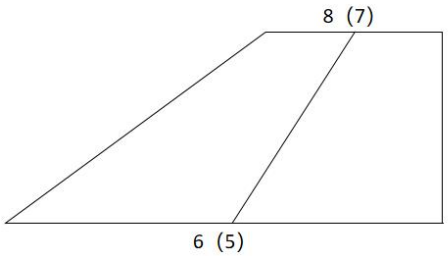

Figure 33 Diagram of the structure monitoring point locations

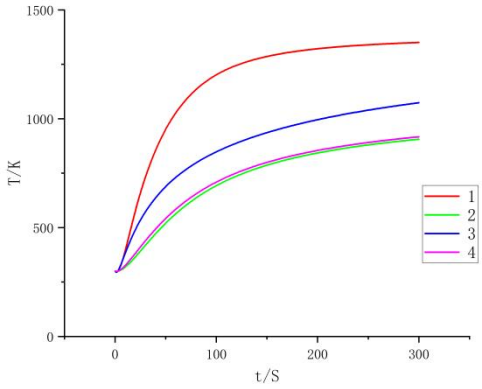

Figure 34 Temperature changes of structural monitoring points

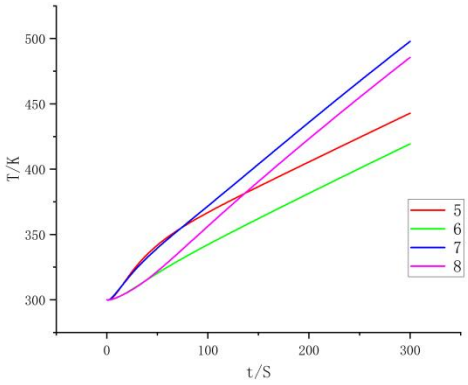

Figure 35 Temperature changes of structural monitoring points

4.2.4 Deformation of rudder structure

Figure 36 and Figure 37 illustrate the temporal evolution of the maximum aeroelastic deformation and maximum thermal deformation of the rudder, respectively. As illustrated in the figures, with the progression of flight time, both the aeroelastic deformation and thermal deformation reach their maximum values at approximately 20 seconds. Thereafter, the thermal deformation exhibits a gradual decline, culminating in a state of stability. In contrast, the aeroelastic deformation initially declines, followed by a resurgence. This is due to the initial heat

flow being considerable, resulting in a sharp rise in surface temperature, which in turn causes an increase in both the aeroelastic deformation and thermal deformation. Once the aerodynamic heating and radiation heat dissipation have reached a balance, the aeroelastic deformation and thermal deformation reach their maximum value. At this point, the surface temperature also tends to stabilise. However, the temperature of the structural layer continues to increase, which results in the aeroelastic deformation continuing to increase after a period of decrease. Due to the differing computational methodologies employed, there is a slight discrepancy between the maximum values of aeroelastic deformation and thermal deformation. The maximum value of thermal deformation is approximately 20 times that of the maximum value of aeroelastic deformation, which illustrates the profound influence of thermal effects on hypersonic vehicles.

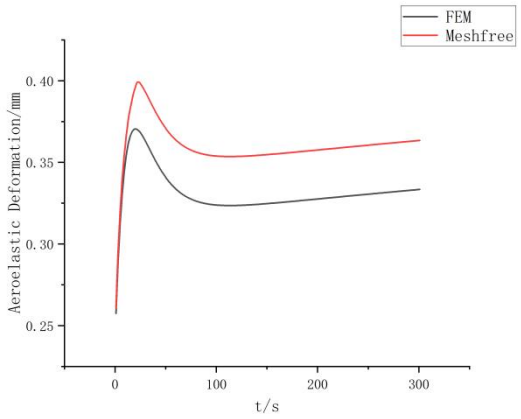

Figure 36 Maximum aeroelastic deformation over time

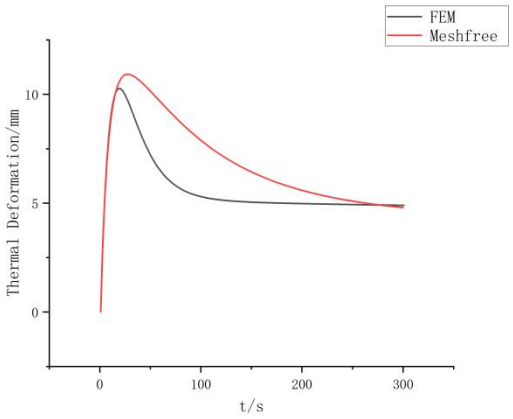

Figure 37 Maximum thermal deformation over time

The aeroelastic and thermal deformation diagrams of the finite element method and meshfree method at 300 s are presented in Figure 38 to Figure 41, respectively. Due to the solid support constraints in the middle of the rudder root, the leading and trailing edges of the rudder will warp to a certain extent. The maximum aeroelastic deformation and thermal deformation will therefore occur at the tip of the leading edge, due to the influence of the aerodynamic forces and the temperature distribution.

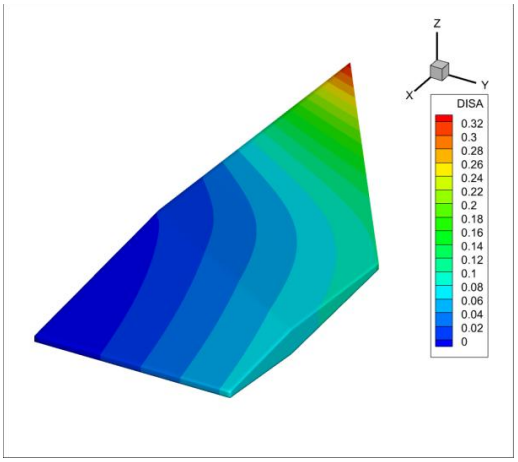

Figure 38 Diagram of aeroelasticity deformation at 300s by FEM

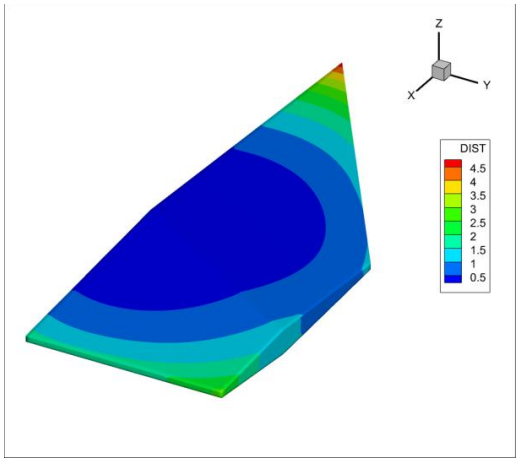

Figure 39 Diagram of thermal deformation at 300s by FEM

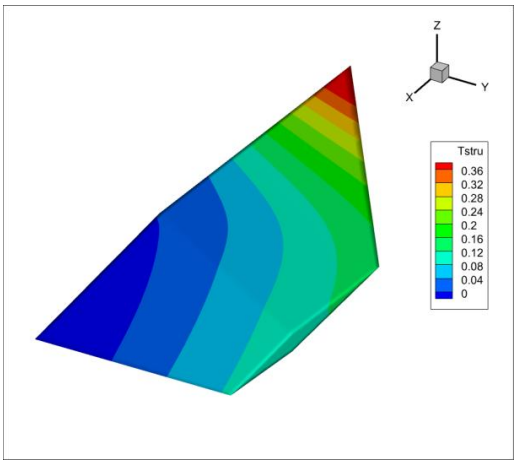

Figure 40 Diagram of aeroelasticity deformation at 300s by meshfree method

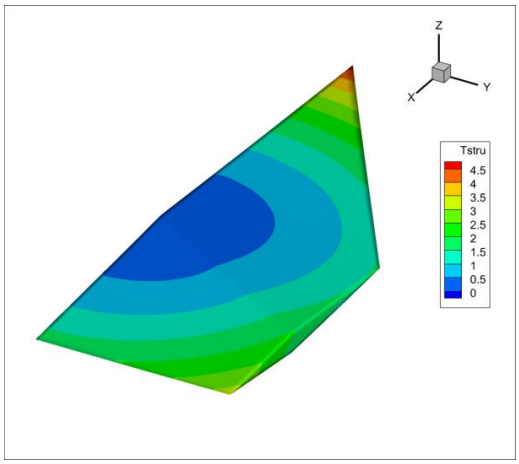

Figure 41 Diagram of thermal deformation at 300s by meshfree method

5 CONCLUSIONS

This paper establishes a framework for the aerodynamic/structural/thermal three-field coupled analysis of hypersonic vehicles and completes the thermal aeroelastic analysis based on the meshfree method for the rudder of a hypersonic missile. A comparison of the results obtained using the traditional finite element method with those obtained using the meshfree method leads to the following conclusion:

(1) The meshfree method improves computational efficiency and saves computation time by pre-storing the stiffness matrix, while ensuring the accuracy of the analysis results.

(2) The analysis results of both the finite element method and the meshfree method demonstrate that the aerodynamic thermal effect is particularly pronounced in hypersonic flight. Thermal deformation is significantly larger than aeroelastic deformation, indicating that the influence of the thermal effect cannot be overlooked in analysing the flight process of a hypersonic vehicle.

REFERENCES

[1] Lighthill M J. Oscillating Airfoils at High Mach Number[J]. Journal of the Aeronautical Sciences, 1953, 20(6):402-406.
[2] Ashley H, Zartarian G. Piston theory—a new aerodynamic tool for the aeroelastican[J]. Journal of the Aeronautical Sciences, 1956, 23(12):1109-1118.
[3] McNamara J J, Crowell A R, Friedmann P P, et al. Approximate Modeling of Unsteady Aerodynamics for Hypersonic Aeroelasticity[J]. Journal of Aircraft, 2010, 47(6):1932-1945.
[4] Meijer, M C, Dala L. Generalized Formulation and Review of Piston Theory for Airfoils[J]. AIAA Journal, 2015:1-11.
[5] DE Jarnette F R, Hamilton H H. Inviscid surface streamlines and heat transfer on shuttle-type configurations[J]. Journal of Spacecraft and Rockets, 1973, 10(5): 314-321.
[6] Ji W D, Wang J F. Calculating method of aerodynamic heating for hypersonic aircrafts[J]. Transactions of Nanjing University of Aeronautics and Astronautics, 2013, 30(3): 327-342.
[7] Culler AJ, Mcnamara JJ. Studies on Fluid-Structural Coupling for Aerothermoelasticity in Hypersonic Flow[J]. AIAA Journal, 2010, 48(8): 1721-1738.
[8] Miller B A, Mcnamara J J. Loosely Coupled Time-Marching of Fluid-Thermal-Structural Interactions with Time-Accurate CFD[J]. AIAA Journal, 2013.
[9] Ji W D, Wang J F. Calculating method of aerodynamic heating for hypersonic aircrafts[J]. Transactions of Nanjing University of Aeronautics and Astronautics, 2013, 30(3): 327-342.

COPYRIGHT STATEMENT